



# In Cellulo Analysis of Huntingtin Inclusion Bodies by Cryogenic Nanoprobe SAXS

Christoph Rumancev,\*<sup>[a]</sup> Tobias Vöpel,<sup>[b]</sup> Susan Stuhr,<sup>[a]</sup> Andreas R. von Gundlach,<sup>[a]</sup> Tobias Senkbeil,<sup>[a]</sup> Markus Osterhoff,<sup>[c]</sup> Michael Sprung,<sup>[c]</sup> Vasil M. Garamus,<sup>[e]</sup> Simon Ebbinghaus,\*<sup>[b, d]</sup> and Axel Rosenhahn\*<sup>[a]</sup>

Huntington's disease (HD) is one of nine neurodegenerative disorders associated with an extension of polyglutamine (polyQ) in proteins. In HD, the polyQ tract in the huntingtin protein is extended beyond a threshold of 38 amino acids leading to the formation of amyloidal structures in the cytoplasm and nucleus. We investigated here the structure of Htt (Huntingtin) amyloid fibrils in cellulo with nanoprobe small angle X-ray scattering. As these measurements were performed under cryogenic conditions, the information is obtained on the aggregates in their natural, hydrated environment without the need of staining

and chemical fixation. We also could show the presence of oligomer structures not visible in fluorescence microscopy. Structural information on repetitive units inside of Htt inclusion bodies was determined from the SAXS data and compared to electron microscopy images. The results suggest that nanoprobe cryo-SAXS can serve as powerful tool to investigate the kinetics of amyloid aggregate formation inside cells and to understand how fibril formation can be influenced by drugs and other external stimuli.

## 1. Introduction

Huntington's disease (HD) is caused by mutation in CAG trinucleotide repeat in the gene IT15 coding huntingtin protein (Htt).<sup>[1]</sup> Htt is ubiquitously expressed in cells. It is involved in embryonal development and neurogenesis,<sup>[2]</sup> endocytosis, intracellular trafficking and membrane recycling,<sup>[3]</sup> but its molecular function is not yet understood<sup>[24],[5]</sup> In healthy conditions, the

exon-1 of Htt (Htt-ex1) encompasses a polyglutamine (polyQ) tract between 1 and 37 glutamine, in disease conditions polyQ units alter between 38 and 180 repeats. [6] Extended proteins aggregate in cells leading to neuronal death and striatal degeneration causing the disease symptoms of HD, including chorea and dementia. The age of onset of the disease decreases and aggregation accelerates with an increased number of polyQ amino acids in Htt.

As a cure for HD is still missing, the understanding of the Htt aggregation pathway on a molecular level is crucial to derive novel therapeutic strategies. As such, small molecules that interfere with the aggregation pathway to prevent aggregation or to redirect aggregation towards non-toxic species were developed for Htt[7] and other amyloid forming proteins like amyloid- $\beta$  (A $\beta$ ) or tau.<sup>[8–10]</sup> For this strategy, precise knowledge of the structure and morphology of the aggregates in the cell is needed. Thereby, it is essential that this knowledge is acquired by in vivo methods since in-cell aggregation is significantly different from what is expected from in vitro measurements in dilute solution or solid matrix. Factors that alter the in-cell aggregation mechanism compared to test tube conditions include biological factors such as molecular chaperones and physicochemical factors such as macromolecular crowdina.

Here we use X-rays to study amyloids with spatially resolved small angle X-ray scattering (nano-SAXS) *in cellulo* on frozen hydrated cells, without chemical staining or fixation. SAXS is an established method to characterize the structure of biomolecules and cells and probes nanostructures with sizes from one up to a few hundred nanometers.<sup>[11]</sup> Protein structures can be studied in solution<sup>[12]</sup> and SAXS was capable to reveal the micro fibril orientation in human bones,<sup>[13]</sup> to determine the antibiotic action for *Escherichia coli* cells,<sup>[14]</sup> and to understand the ultrastructure of melanosomes.<sup>[15]</sup> Periodic structures in living

- [a] Dr. C. Rumancev, Dr. S. Stuhr, Dr. A. R. von Gundlach, Dr. T. Senkbeil, Prof. Dr. A. Rosenhahn Analytical Chemistry – Biointerfaces Ruhr University Bochum Universitätsstr. 150, 44780 Bochum (Germany) E-mail: christoph.rumancev@rub.de axel.rosenhahn@rub.de
- [b] Dr. T. Vöpel, Prof. Dr. S. Ebbinghaus Department of Physical Chemistry II Ruhr University Bochum Universitätsstr. 150, 44780 Bochum (Germany) E-mail: s.ebbinghaus@tu-braunschweig.de
- [c] Dr. M. Osterhoff, Dr. M. Sprung Deutsches Elektronen-Synchrotron DESY Notkestr. 85, 22607 Hamburg (Germany)
- [d] Prof. Dr. S. Ebbinghaus Institute of Physical and Theoretical Chemistry TU Braunschweig Rebenring 56, 38106 Braunschweig (Germany)
- [e] Dr. V. M. Garamus Helmholtz-Zentrum Geesthacht: Centre for Materials and Coast Research Institute of Materials Research Max-Planck-Str. 1, 21502 Geesthacht (Germany)
- Supporting information for this article is available on the WWW under https://doi.org/10.1002/syst.202000050
- An invited contribution to a Special Collection on the Chemistry of Crowded Systems
- © 2020 The Authors. ChemSystemChem published by Wiley-VCH GmbH. This is an open access article under the terms of the Creative Commons Attribution Non-Commercial License, which permits use, distribution and reproduction in any medium, provided the original work is properly cited and is not used for commercial purposes.



eukaryotic cells were successfully analyzed nanodiffraction.[16] We applied nano-SAXS to detect the internal amyloid structure of inclusion bodies and to estimate the size of repetitive units within the aggregates for the first time in cellulo. In addition to Q72 we compared Q25 transfected and non-transfected cells to understand the structural difference caused by the different polyQ lengths. While conventional imaging methods rely on labeling or histological staining to detect amyloid plagues, X-rays are intrinsically sensitive to such periodic structures resulting from the secondary, tertiary and quaternary structures of proteins. Staining and labelling are not required for such X-ray experiments and the X-ray nanoprobe experiment allowed to reveal the local distribution and the size of amyloid structures within frozen-hydrated cells.

#### 2. Material and Methods

#### 2.1. Cell Culture and Transfection

HeLa cells used in this study were a kind gift from the Department of Biochemistry II (Ruhr-Universität Bochum) and were cultured in DMEM (Gibco, USA) supplemented with 10% fetal bovine serum (Sigma Aldrich Chemie GmbH, Germany) and 1% penicillin-streptomycin (Gibco, USA) at 37°C and humidified atmosphere with 5% CO<sub>2</sub> using T-25 cell culture flasks (Sarstedt AG & Co, Germany). At 80% confluence the cells were transfected with 2 µg of DNA of IRES constructs containing Htt-ex1 polyQ n-mCerulean and Htt-ex1 polyQ n-mYFP<sup>[1]</sup> with different polyglutamine lengths (Q25, Q72). Lipofectamine 2000 (Life Technologies GmbH, Germany) was used as the transfection reagent following the manufactures protocol. Then 6 hours post transfection the 7,500-10,000 cells were split and seeded onto copper TEM grids covered with a carbon surface with a 200 mesh (Quantifoil Micro tools GmbH). After splitting cells were cultivated for another 12-16 hours prior to imaging.

### 2.2. Fluorescence Microscopy and Cryo-fixation

The different transfected cells were seeded onto TEM grids membranes and allowed to adhere for 12 h. After this incubation time, cells were imaged using a Zeiss Axio Observer Z1 (Zeiss Microscopy GmbH, Germany) fluorescence microscope. Cells containing aggregates were identified using overlay images of the FRET fluorescence channel (Emission range: 530–600 nm) and the transmission channel. Immediately after acquisition of the microscopy images, the liquid was blotted from the TEM grids with cellulose paper (Whatman grade No. 1) and the samples were plunge frozen<sup>[17]</sup> in a mixture of 37% liquid ethane and 63% liquid propane at liquid nitrogen temperature. The cryogenically fixed samples were stored in liquid nitrogen until the beamtime. For SAXS measurements, suitable cells were selected based on light microscopic and fluorescence microscopy images.

#### 2.3. SAXS Measurements

SAXS measurements were carried out at the P10 beamline (PETRA III, DESY), using the Göttingen Instrument for Nano Imaging with X-rays (GINIX)[18-20] equipped with a cryojet (Cryojet, Oxford Instruments, UK) to maintain the sample at 100 K. Photons with an energy of 7.9 keV were focused on the sample with a spot size of 300x300 nm<sup>2</sup>. The flux on the sample was  $\approx 10^{11}$  ph/s. Scattering patterns were collected with an Eiger 4 M single photon counting detector (Dectris, Switzerland) which recorded scattering vectors between 0.0045 Å<sup>-1</sup> and 0.111 Å<sup>-1</sup>. To protect the detector from the direct beam, a semitransparent beam stop was used. Spatially resolved scattering data was recorded by scanning the sample through the Xray focus. Different step sizes of  $0.25 \times 0.25 \,\mu\text{m}^2$ ,  $2 \times 2 \,\mu\text{m}^2$  and  $1 \times 1 \mu m^2$  with an exposure time of 1 s were used. The step size of  $0.25 \times 0.25 \,\mu\text{m}^2$  revealed the highest spatial resolution but was time consuming, the step sizes of  $1 \times 1 \mu m^2$  and  $2 \times 2 \mu m^2$ revealed reasonable resolution while acquisition times were shorter.

### 2.4. Calculation of SAXS Curves

To preview the spatially resolved scattering data, the average scattering intensity of the entire q-range was used to calculate phase contrast maps (Figure 1). Regions of interest (ROI) in the STXM images were identified by correlation with light microscopy and fluorescence images, and labelled as area 1, area 2, and area 3. While area 1 contained aggregates, area 2 did not. Area 3 is the supporting carbon membrane as background reference. For Q25 cells that did not show aggregate formation, similar intracellular regions of similar size were selected for comparative analysis. Within the three regions of interest, the scattering patterns were averaged and converted into scattering curves by radial averaging (see also extended explanation in the supplementary material). This extraction was done by using the IRENA macros<sup>[21]</sup> for Igor Pro (Wavemetrics, Portland, USA). The scattering vector q was calculated as  $q = \frac{4\pi}{3}\sin(\theta)$ , with  $\lambda$  being the X-ray wavelength and  $\theta$  half of the scattering angle. Before the analysis, the obtained SAXS curves were normalized to the q-range between 0.06  $\text{Å}^{-1}$  and 0.08  $\text{Å}^{-1}$ . In this range, the SAXS curves showed a similar curve shape with limited structural information. The final SAXS curves of Q25 Httex1 area 1 contain the averaged information of the ROIs of 8 single scattering patterns and Q25 Htt-ex1 area 2 the information of 15 single scattering patterns. The final SAXS curves of Q72 Htt-ex1 area 1 contains 12 single scattering patterns and Q72 Htt-ex1 area 2 contains 8 single scattering patterns (See S1).

## 2.5. Analysis of SAXS Data

In order to extract structural information about the investigated intracellular regions from the scattering curves, two different methods of data analysis were applied: the Guinier-Porod



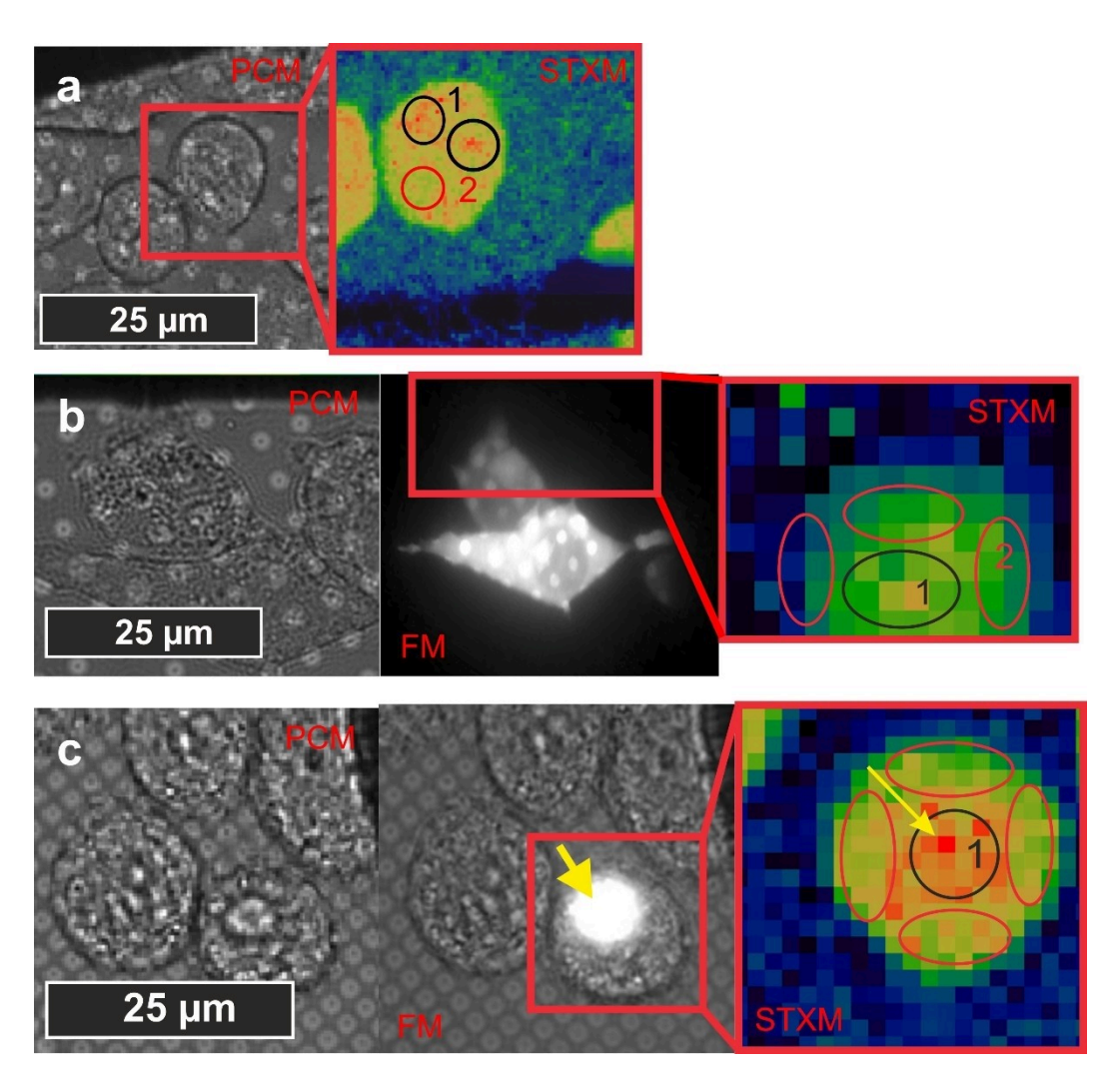


Figure 1. Phase contrast microscopy (PCM), fluorescence microscopy (FM), and STXM images of the investigated cells with different Htt-ex1 aggregation formation. (a) HeLa cells without Htt-ex1 (non-transfected), PCM and STXM (STXM:  $0.5 \,\mu\text{m} \times 0.5 \,\mu\text{m} \times 0.5 \,\mu\text{m} \times 40 \,\mu\text{m} \times 40 \,\mu\text{m}$  image size). (b) HeLa cells with Q25 Htt-ex1 but free of visible Htt aggregates, PCM, FM, and STXM (STXM:  $2 \,\mu\text{m} \times 2 \,\mu\text{m}$  step size,  $28 \,\mu\text{m} \times 18 \,\mu\text{m}$  image size). (c) HeLa cells with Q72 Htt-ex1 which form Htt aggregates, PCM, FM, and STXM (STXM:  $1 \,\mu\text{m} \times 1 \,\mu\text{m}$  step size,  $21 \,\mu\text{m} \times 21 \,\mu\text{m}$ ). The location of aggregates in (c) becomes apparent in both, PCM and FM images (aggregates are indicated by the yellow arrow). The red rectangle in the microscopy images indicates the area analyzed by microprobe SAXS. The red and black circles in the STXM images show regions selected for a detailed SAXS analysis. Black circles (area 1) show areas with high scattering intensity and red circles (area 2) indicate the cell body areas with lower scattering intensity.

analysis<sup>[22]</sup> and an indirect Fourier transformation method to retrieve p(r)-distribution functions. [23] Both approaches were compared to enhance self-consistency of the data analysis and to approximate size and shape of the Htt-ex1 aggregates. For the analysis by the Guinier-Porod method, SAXS intensities between 0.005  $\text{Å}^{-1}$  and 0.03  $\text{Å}^{-1}$  were considered. The *q*-range was smaller than the recorded one in order to disregard very large scattering vectors that were dominated by noise and to cut out artifacts introduced by the beam stop at low q-values. In the case of Q25 and non-transfected (NT) cells, it was possible to fit the data by a simple Porod decay,[22] which is simply the slope of the curve. In the case of local intensity increases below a certain q-value  $q_1$ , like in the case of the Q72 cells, a simple Porod-analysis could only be used for  $q \ge q_1$ . Here a generalized Guinier-Porod model<sup>[22]</sup> for nonspherical objects was applied to model the data [Equations (1), (2)]:

$$I(q) = \frac{G}{q^s} exp\left(\frac{-q^2 R_g^2}{3-s}\right) \text{ for } q \le q_1$$
 (1)

$$I(q) = \frac{D}{q^d} \text{ for } q \ge q_1$$
 (2)

with 
$$q_1 = \frac{1}{R_g} \left[ \frac{(d-s)(3-s)}{2} \right]^{1/2}$$
,

I(q) is the measured scattering intensity, q the scattering vector, D the Porod scale factor and d the Porod exponent, G is the Guinier scale factor,  $R_g$  is the radius of gyration of the scattering object (radius gyration of cylindrical cross section for rod-like or radius gyration of thickness for flat objects) and s a variable that contains its shape information. In the case of spherical objects, s values are equal to 0, while for non-spherical



objects s=1 for rod or cylindrical structures and s=2 for lamellar or plate like objects.

An alternative way to analyze the scattering data is a model independent indirect Fourier transformation which allows to calculate pair distance distribution functions-p(r). To calculate the p(r)-function directly from the scattering curves, the PRIMUS/qt<sup>[24]</sup> software was used, which is a part of ATSAS software package. To become able to consistently apply the indirect Fourier transformation, the  $D_{max}$  values were iteratively adapted to obtain the best fit of the experimental data and a stable solution for the p(r)-function, being a linear combination of K orthogonal functions  $\varphi(s)^{[12]}$  between 0 and  $D_{max}$  [Equation (3)]:

$$p(r) = \sum_{k=1}^{K} c_k \varphi_k(r) \tag{3}$$

This pair distance distribution function can be considered as histogram of the sizes of specific substructures that cause the enhanced scattering signal.[12] In the case of homogeneous objects, the p(r) function contains the occurrence of all interatomic distances within the investigated object with a maximal distance  $D_{max}$  that corresponds to the diameter of the particle (cross section diameter for rod-like or thickness for flat particles). The shape of the p(r) function provides information about the shape of the scattering objects and the distribution of scattering length densities within them. From the p(r)function, the radius of gyration (R<sub>q</sub>) of excess of scattering length density within the particles (cylindrical cross section or thickness) can be determined. The error bars in the p(r) function represent error propagations performed via a series of Monte-Carlo simulations which allow to add the standard deviations to the points of the p(r) function as well as to the derived values such as the radius of gyration and zero-angle intensity.

# 3. Results

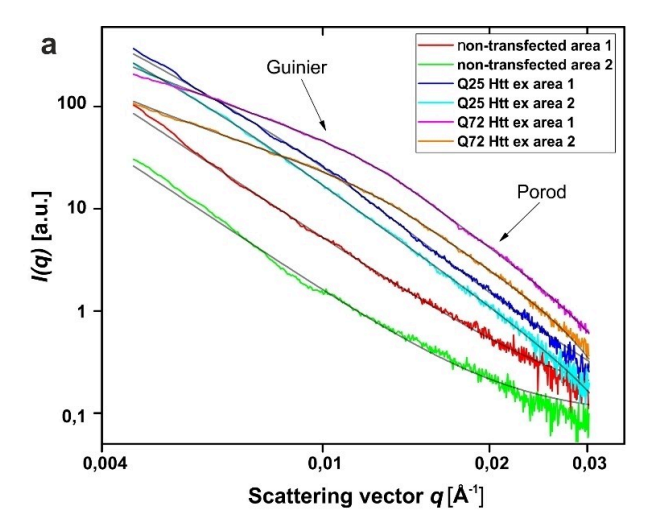
To establish nanoprobe small angle X-ray scattering (nano-SAXS) as a tool to study intracellular aggregation processes, we overexpressed Htt-ex1 with different polyglutamine lengths (Q25, Q72). We used exon-1 instead of the 3144 amino acid long full length protein since exon-1 is sufficient to induce an HD-like phenotype in transgenic mouse models. [26] Htt-ex1 Q25 transfected cells showed no aggregates while Htt-ex1 Q72 transfected cells developed visible aggregates with an average size of several  $\mu m$  12–16 hours post transfection (Figure 1 a–c). To distinguish transfected from non-transfected cells, Htt-ex1 was labelled with a fluorescent dye. To preserve the cells for the SAXS measurements, the samples were plunge frozen immediately after recording the microscopy images in a liquid ethane/ propane mixture and stored in liquid nitrogen.[17,27] During the nano-SAXS measurements, a cryo-jet was used to keep the temperature of the frozen hydrated samples at 100 K. With this approach we were able to investigate the aggregates in a frozen-hydrated state while conserving the intracellular structures. Among the advantages of cryofixation is that cells are embedded in amorphous ice without any crystallization of water. Thus, the intracellular structures are maintained similarly to their natural, hydrated condition. Another advantage of cryo preparation is the minimization of structural changes due to radiation damage (e.g. mass loss or bubble formation).<sup>[28]</sup> As the amorphous ice layer reduces such effects, it is a frequently used preparation method for the investigation of biological samples like cells at synchrotron sources<sup>[29–31]</sup> and in electron microscopy.<sup>[32–34]</sup>

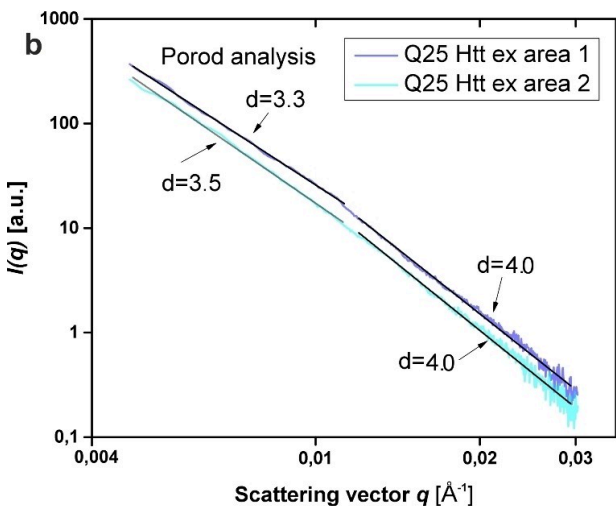
In Figure 1 a-c, light microscopy images and fluorescence microscopy images are shown. In addition, the panels contain X-ray scattering contrast images that were calculated from the average intensity of the scattering patterns. As the direct transmission was blocked by a beam stop, the obtained images contain similar information as conventional phase-contrast scanning transmission X-ray microscopy (STXM) images. The comparison of the phase contrast and fluorescence microscopy images with the STXM data allows to identify regions containing Htt-ex1 aggregates (Figure 1 a-c). The fluorescence images show a homogeneously distributed fluorescence signal in Q25 cells, while in Q72 cells the signal indicates the presence of aggregated Htt-ex1 in highly localized positions. The regions marked in Figure 1 a-c were used to extract the scattering information. Therefore, all scattering patterns that were recorded within the marked areas of interest were summed up and converted into a single scattering curve by radial averaging of intensities. The scattering from cell-free parts of the supporting carbon membrane was used for background correction.

The obtained scattering curves are shown in Figure 2a, two SAXS curves were obtained for each sample. The analyzed regions of interest for area 1 are labelled non-transfected area 1, Q25 Htt-ex1 area 1, Q72 Htt-ex1 area 1 and for area 2 nontransfected area 2, Q25 Htt-ex1 area 2, Q72 Htt-ex1 area 2. For Htt-ex1 Q72 we detected an increase in the scattering intensity between 0.01  $\mathring{A}^{-1}$  and 0.03  $\mathring{A}^{-1}$  in both, area 1 and area 2, compared to the non-aggregate forming controls (NT, Q25). Scattering data for all samples were lacking a plateau at lowest q values that indicates the absence of a Guinier region (Eq.1, s = 0). It allowed us to conclude that the size of the investigated objects was larger than the captured q-range, i.e.  $> 2\pi/q_{min} =$ 1400 Å. The obtained scattering signal was thus caused by parts of whole aggregates or interfaces. The analysis was continued with a determination of the parameter d (Equation 2) for the entire curve or parts of it. In the case of NT cells (Figure 2a), the whole curve can be approximated with a slope ~3.6 which indicates scattering at interfaces of large, fractal-like objects. In such a case, the ratio between the surface of the object (S) and its linear size (I) is  $S \sim I^{6-d}$ . [35]

For transfected cells (Figure 2 b and c), the situation is more complicated and the two different q-ranges in the Q25 and the Q72 curves were analyzed as two separate Porod-decays and different slopes were obtained (Table 1). Q25 curves show a slope d of 3.3 and 3.5 at q values between 0.005 Å $^{-1}$  and 0.01 Å $^{-1}$  and d=4.0 for larger q values. This can be interpreted as Q25 cells scattering at length scales larger than  $\sim$  300 Å from fractal surfaces of large objects and at length scales smaller







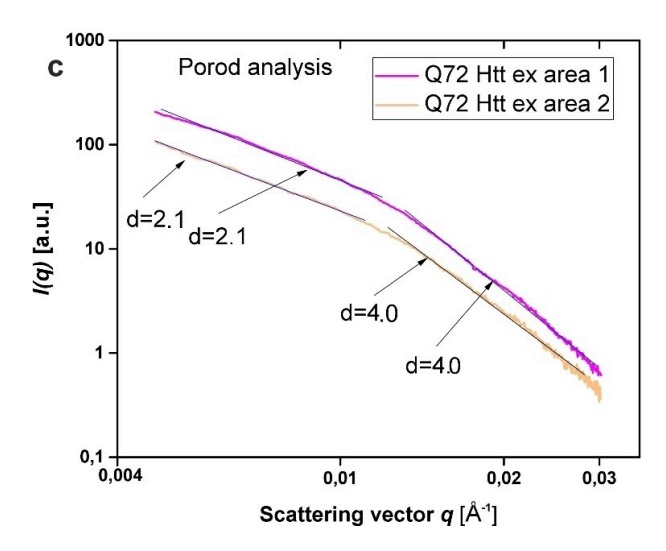


**Figure 2.** (a) SAXS curves of HeLa cells: NT (non-transfected) without Htt-ex1, Q25 and Q72 Htt-ex1, used in the size analysis by Guinier-Porod and p(r) functions. (b), (c) Porod analysis of area 1 and area 2 in Q25 and Q72 cells. Each curve is separated into two regions. Whereas the Porod slopes in both parts of the Q25 curves deviate slightly, it deviates strongly in the case of Q72. The additional contribution was accounted for by the introduction of a Guinier-contribution. All curves used in the analysis are presented in the supporting information Figure S2.

**Table 1.** Summary of the results of the Porod analysis for the different cell types and regions of interest. d values are the Porod exponents either for the full curve or for  $q > q_1$ .

non-transfected area 1 $3.6 \pm 0.1$ non-transfected area 2 $3.5 \pm 0.1$ Q25 Htt-ex1 area 1 $3.3 \pm 0.1$ $4.0 \pm 0.1$ Q25 Htt-ex1 area 2 $3.5 \pm 0.1$ $4.0 \pm 0.1$
Q25 Htt-ex1 area 1 $3.3 \pm 0.1$ $4.0 \pm 0.1$
035 Htt 0x10x00 3
Q25 Htt-ex1area 2 $3.5 \pm 0.1$ $4.0 \pm 0.1$
Q72 Htt-ex1 area 1 2.1 $\pm$ 0.1 4.0 $\pm$ 0.1
Q72 Htt-ex1 area 2 $2.1 \pm 0.1$ $4.0 \pm 0.1$

than 100 Å from objects with smooth and well defined interfaces (slope 4, classical Porod behavior). Thus, small objects with sizes of  $\approx$  100 Å form larger objects with fractal interfaces and so-called primary particles build the larger fractal objects. Q72 curves show a slope d of 2.1 at q between 0.005 Å<sup>-1</sup> and 0.01 Å<sup>-1</sup> and d=4.0 for larger q values. A slope of 2.1 suggests scattering from objects like volume fractals or scattering from large, flat objects with diameters larger than 1400 Å. For length scales less than 100 Å, scattering arose from smooth and sharp surfaces. Q72 curves show a rather clear transition of the d values from 4 to 2.1, while the change from 4 to 3.3/3.5 in Q25 is less pronounced.

In order to derive structural and size information from this Guinier region with enhanced scattering intensity, a Guinier-Porod (GP) approach was used. The scattering curves of nontransfected cells (NT) and of Htt-ex1 Q25 transfected cells are well described by Porod's law, i.e. the exponential slope of the SAXS-curves. In the case of the Q72 cells, a simple Porod model was not appropriate to describe the shape of the curve due to an additional scattering contribution at  $q \approx 0.013 \, \text{Å}^{-1}$ . Latter was considered by applying the GP model which provides in addition to the Porod decay a Guinier function that describes such an additional scattering contribution. From the analysis, radius of gyration  $R_g$  and s values are obtained (Table 2) which characterize the scattering contribution in terms of size and shape, respectively.

The parameter s obtained from the GP model helps to estimate the shape of the scattering object and typically spherical shapes yield s=0, rod-like or cylindrical structures s=1, and lamellar structures s=2. For both areas of Q72, s values of 2 were obtained which suggests the presence of flat, lamellar structures. The  $R_{T,g}$  (radius gyration of thickness) values for these structures were determined as  $R_g=56$  Å for Q72 Htt-ex1 area 1 and for area 2  $R_g=49$  Å. Assuming homogeneous and flat particles, the thickness T was calculated as

**Table 2.** Summary of the results for the Q72 transfected cells after fitting a Guinier-Porod (GP) model. s-values indicate the shape of the scattering objects as determined from the Guinier analysis.  $R_g(GP)$  resembles the radius of gyration as obtained from the GP model and T(GP) the corresponding thickness of the structures. For both areas s=2 were determined.

Sample	S	$R_{T,g}(GP)$ [Å]	Thickness T(GP) [Å]
Q72 Htt-ex1 area 1	2	56±1	193±3
Q72 Htt-ex1 area 2	2	$49\pm1$	$169\pm4$

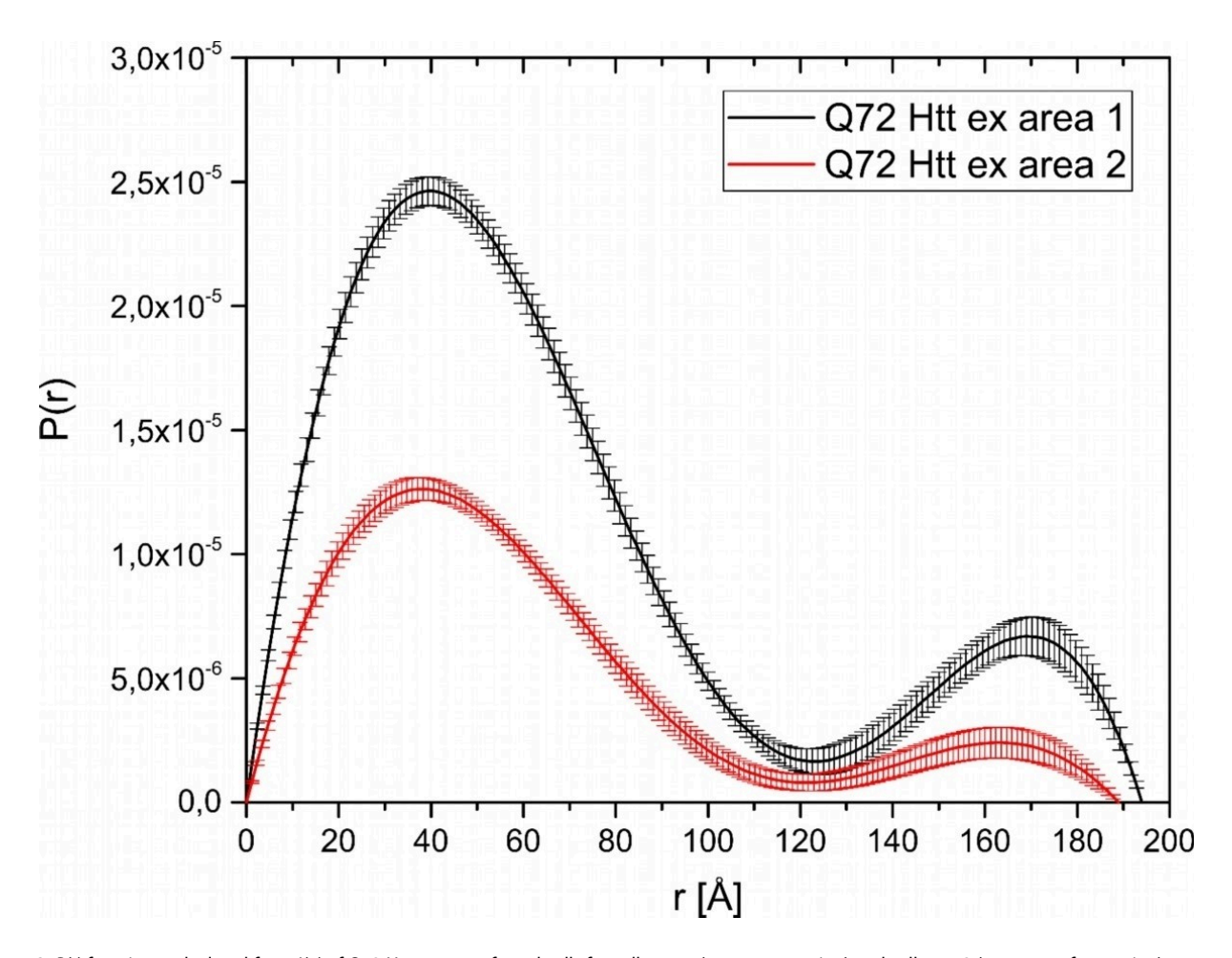


Figure 3. P(r) functions calculated from I(q) of Q72 Htt-ex1 transfected cells for cell area 1 (aggregate region) and cell area 2 (aggregate free region).

 $T = R_g^* \sqrt{12}$ , [22][36] resulting in T = 193 Å for area 1 and T = 169 Å for area 2. In Table 2, values for s,  $R_g$ , and T are summarized.

An alternative way to analyze the scattering data and to obtain additional information about the shape of the aggregates is the calculation of a pair distance distribution function using an indirect Fourier transformation (IFT) method as implemented in PRIMUS/qt<sup>[24]</sup> from the ATSAS software package. [25] p(r) was calculated under the assumption of flat, monodisperse particles as derived from the GP analysis and as a result, profiles p(r) of the scattering objects with bimodal distribution were obtained (Figure 3). From the p(r) curves, the radius of gyration of thickness  $(R_{T,g})$  and  $D_{max}$  values were obtained (Table 3). For Q72 Htt-ex1 aggregates (Q72 Htt-ex1 area 1) a radius of gyration of  $R_{T,g}(p(r)) = 57$  Å was determined and for the regions lacking visible aggregates (Q72 Htt-ex1 area 2)  $R_{T,g}(p(r)) = 52$  Å. Both values are very similar to the ones

**Table 3.**  $R_{T,g}$ ,  $T_i$  and  $D_{max}$  values derived from the Indirect Fourier Transformation analysis. For the calculation, a flat shape of the aggregates has been assumed.

	$R_{T,g}(P(r))$ [Å]	T(P(r)) [Å]	$D_{max}$ [Å]
Q72 Htt-ex1 area 1	58 ± 1	199±5	194
Q72 Htt-ex1 area 2	$52\pm1$	$180\pm5$	189

obtained from the GP analysis. The iteratively determined maximal distances  $D_{max}$  within scattering objects are 194 Å and 189 Å, respectively. Thus, GP-analysis and p(r)-function indicate the presence of flat objects with thicknesses of  $\approx$  190 Å. Here it is important that  $D_{max}$  is the thickness of the objects "visible" in this SAXS experiment. Whole agglomerates on the micrometer length scale as visible in the phase contrast and fluorescence microscopy images are much too large for the q-range accessible by SAXS.

# 4. Discussion

The analysis using Porod's law fits the slope of the scattering curves and provides the exponent d which contains information about the internal organization of the sample in the investigated field of view. In general, Porod exponents close to  $d\approx 4$  are typical for homogeneous objects with a smooth and sharp surface, while decreased d values indicate a granulation of the surface and/or the internal structures. [37,14] In Figure 4, the d-values for different object shapes are illustrated. For the nontransfected cells, the analysis of the scattering data using Porod's law resulted in d values of 3.5 (Table 1). The Q25 and Q72 SAXS curves contained two different Porod slopes (Fig-

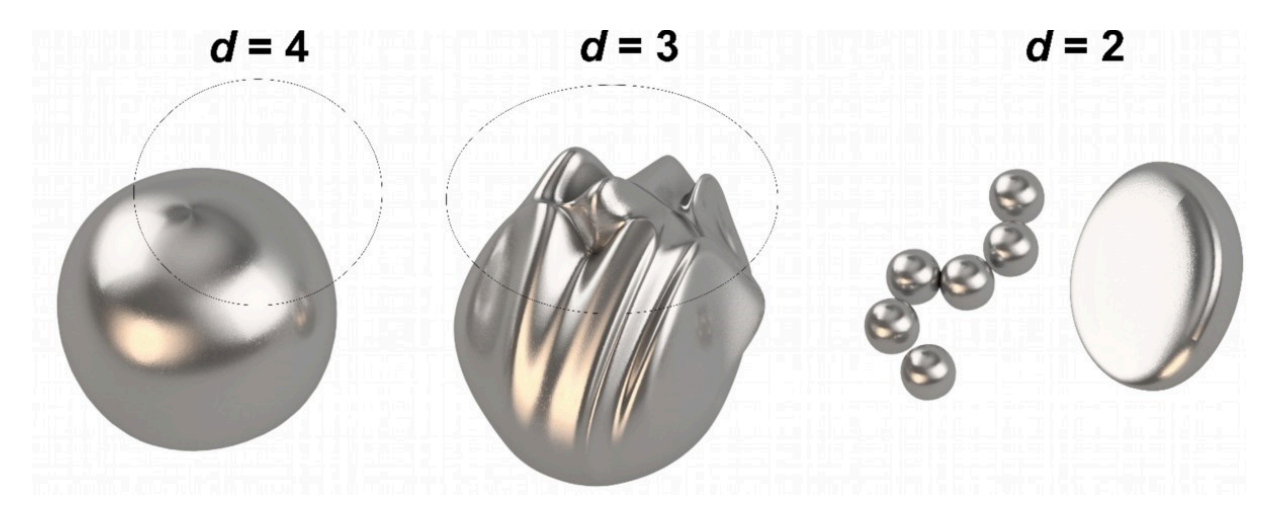
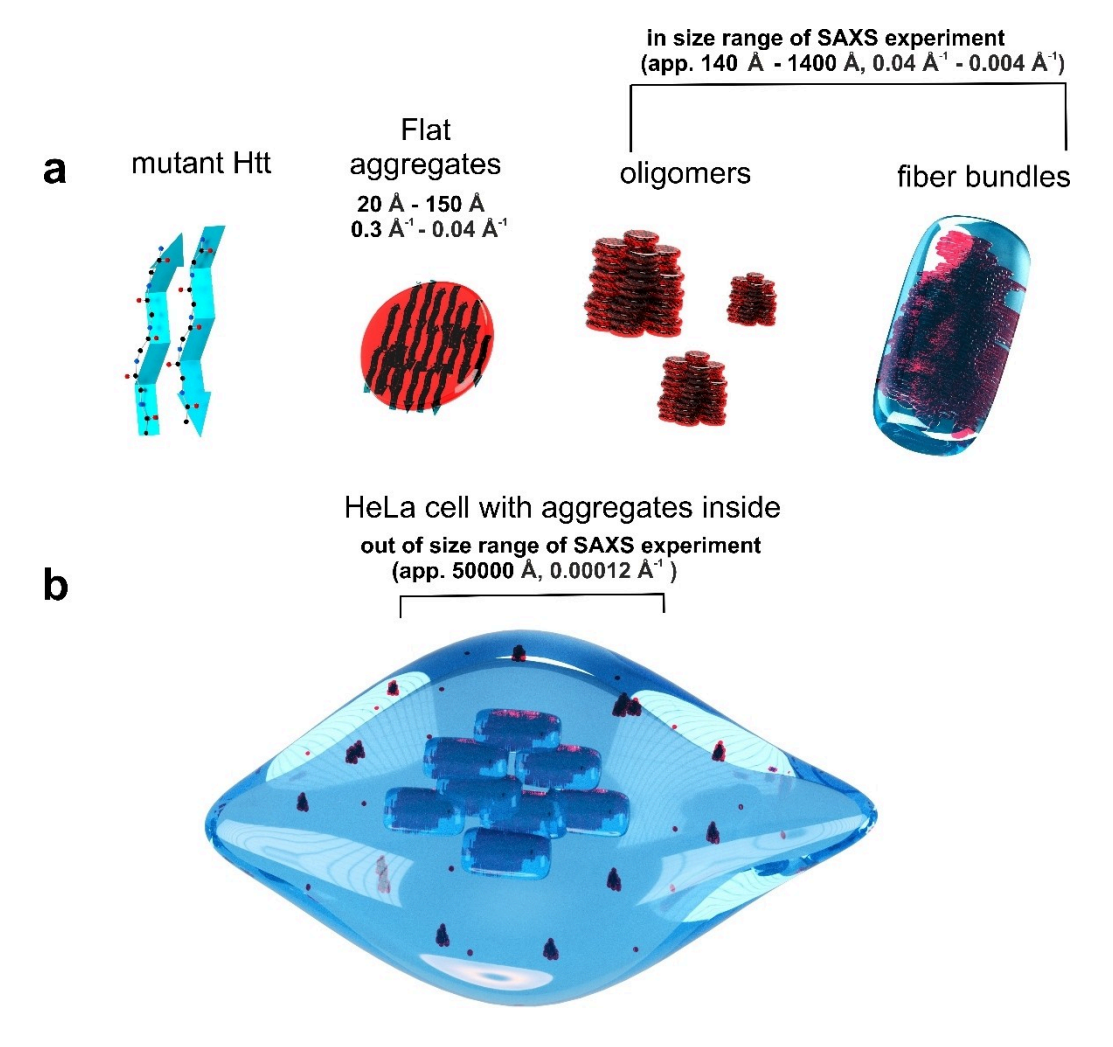


Figure 4. Schematic illustration of *d* values for different object shapes. *d*-values of 4 at large *q* are typical for objects with smooth and sharp interfaces. A decrease of *d* to values between 3 and 4 signifies granulation of the interface of the objects – the surfaces shows additional structure, e.g. roughness. *d*-Values of 2 are typical for small objects like proteins which can form flat sheet like structures or Gaussian chains, here a Guinier plateau might occur in the SAXS curves

ure 2). In Q25 Htt-ex1 area 1 and 2 the slope d increased from 3.5 at q between 0.004 Å $^{-1}$  and 0.01 Å $^{-1}$  to d=4.0 for larger q values between 0.01 Å $^{-1}$  and 0.03 Å $^{-1}$  without a noticeable Guinier plateau. d-values of 4 at small q-values indicate the presence of larger structures  $^{[38]}$  or surface fractals with sharp interfaces which are part of structures outside of the measured range. Such structures could be larger aggregates such as those visible in light microscopy images (Figure 1). The analysis of the Porod slopes shows that the transfection of the HeLa cells with Q25 and Q72 induces a transition from a homogeneous interior of the cells towards the formation of intracellular, granular objects.

In both, area 1 and area 2 of the Q72 transfected cells, the slope of the curves d increased from 2.1 between 0.004  $Å^{-1}$  and 0.01  $\text{Å}^{-1}$  up to 4.0 for larger *q*-values between 0.01  $\text{Å}^{-1}$  and 0.03  $\text{Å}^{-1}$ . d-values of 2 can indicate the presence of structures like lamellae or flat discs (Figure 4). In addition to the determination of the d-values, the GP analysis provides  $R_{qr}$  and svalues. From the obtained s values of 2, we deduced that the investigated intracellular structures in Q72 Htt-ex1 area 1 and Q72 Htt-ex1 area 2 are dominated by flat, lamellar objects. Based on this result, the analysis of the p(r) function was done assuming flat and monodisperse particles and a bimodal distribution was obtained (Figure 3). The bimodal distribution could indicate aggregation of the flat objects into two distinct slab thicknesses. The p(r) analysis provides information about the thickness of the flat structures but not about the size of entire objects as the q-range of the SAXS experiment is limited. Both, GP and p(r) analysis provide radii of gyration of thickness of the flat, lamellar objects which were 56 and 49 Å for the GP analysis which agreed very well with the values of 58 and 62 Å obtained by the p(r) analysis. From these numbers, the thickness of the flat, lamellar objects can be calculated to be  $\approx$  190 Å. The obtained data can be interpreted in such a way that flat structures were formed out of stacked ß-sheets during the formation of Huntingtin aggregates with thicknesses of  $\approx$  190 Å. These flat structures can further agglomerate to form multilayers as indicated by the p(r) analysis. This aggregation pathway derived from the SAXS results is illustrated in Figure 5. Stacked ß-sheet structures could be part of amyloidal intermediates (oligomers) which are often discussed in literature as a primer contributor to neuronal cell death. [39]

Even in the areas where the Q72 Htt-ex1 cells did not show obvious aggregate formation, a scattering contribution between  $q \approx 0.01$  and  $q \approx 0.012 \, \text{Å}^{-1}$  was observed that was not present in the Q25 Htt-ex1 cells. While scattering curves measured from the Q25 Htt-ex1 cells were well described by a simple Porod decay, the modeling of the Q72 regions lacking obvious aggregates required the consideration of a Guiniercontribution. Our data suggests that even in those regions of Q72 cells where aggregates are not fully established and not yet visible in light microscopy, pre-formed lamellar structures are already present. From the Guinier-Porod analysis  $R_{T,q}(GP) =$ 49 Å was obtained and from the pair-distribution analysis  $R_{T,q}(p(r)) = 52 \text{ Å and } D_{max} = 189 \text{ Å were obtained for Q72 area 2.}$ In the case of Q72 area 1,  $R_{T,q}(GP)$  show an  $R_{T,q} = 56 \text{ Å}$  and the pair-distribution analysis  $R_{T,a}(p(r)) = 57 \text{ Å}$  and  $D_{max} = 199 \text{ Å}$ (Table 2 and 3). Based on these values and assuming a flat shape, the thickness T of the particles was calculated as  $T = R_{T,a}^* \sqrt{12}$  (Table 2 and 3). The thickness T calculated from GP (193 Å and 169 Å) and *p(r)* (199 Å and 180 Å) are very similar to the real space  $D_{max}$  values (194 Å, 189 Å) which supports the interpretation of the presence of flat, lamellar structures'. [40][41] The bimodal distribution of p(r) analysis indicates the agglomeration of the flat objects in both regions. Fluorescence microscopy images of the Q72 cells show that the fluorescence signal is only occuring in area 1, while in area 2 no fluorescence signal and no obvious aggregates are present. The fluorescence data is in line with the reduced intensity in the SAXS curves of the aggregate-free region (area 2) compared to the region with



**Figure 5.** (a) Sketch of Huntingtin aggregate formation as derived from the SAXS results. The agglomeration starts from soluble oligomers of mutant Htt-ex1. The aggregation starts form mutant Htt-ex1, which forms flat preaggregated structures, these flat structures form oligomers that form larger fibrillary structures and fiber bundles. (b) Illustration of intracellular organization of the aggregates.

aggregates present (area 1). However, it is important that SAXS detected aggregate formation in area 2 with similar structural characteristics as in the Huntingtin aggregates, which suggests the presence of pre-aggregated structures in area 2. As conclusion, the detailed analysis of the fluorescence microscopy and the nano-SAXS data suggest that Q72 Htt-ex1 expression leads not only to the formation of clearly visible aggregates but additionally to pre-formed assemblies within the cytoplasm.

The ultrastructural information gained from the nano-SAXS measurements can be compared to literature results using other analytical methods like AFM or electron microscopy. Dahlgren et al. studied the fibril formation of Q67 Htt-ex1 in vitro. They showed by atomic force microscopy (AFM) that the height of Htt amyloid fibrils is 50 Å at the tip and 110 Å in the middle. Furthermore, they suggested a model of fibrils formed of  $\beta$ -sheet stacks, oriented antiparallel to the fibril axis. This literature result could explain the similar sizes that we determined in the  $\beta$  and in the  $\beta$  and in the  $\beta$  and in the  $\beta$  and the  $\beta$ 

sizes. They proposed an aggregation pathway which starts from the mutant proteins with an abnormal conformation. These proteins could form oligomers with a spherical shape with heights between 20 Å and 150 Å. These oligomers then agglomerate into fibrils, inclusions, and amorphous aggregates (shapeless nuggets). Alternatively, the mutant proteins can directly agglomerate into amorphous and annular (donut shape) aggregates. These aggregates consist of fiber bundles and could reach diameters of up to 10,000 Å. Several other studies support this model, that describe the growth of spherical, annular, fibrillar and amorphous structures. [43-45] The presence of a variety of sizes and shapes could be explained by ß-sheet modes proposed by Dahlgren<sup>[40]</sup> and Der-Sarkissian.<sup>[41]</sup> AFM experiments by Legleiter et al.[46] revealed that mutant Htt can form spherical oligomers  $\approx\!20\text{--}100\,\text{Å}$  in size which are considered to be precursors for large fibrils or amorphous aggregates. At a polyQ length of Q53, no increase of the oligomer concentration was observed before fibrils are formed, which is indicative for a fast formation kinetics. Further, the formation of annular structures with different sizes is also



possible for mutant Htt. The derived model fits very well to the above described model of *Burke et al.* [42] As electron microscopy or AFM are not applicable in the cellular setting, structural insights in the native cellular environment remain sparse. Super resolution microscopy allowed to image fluorescently labelled Htt in the cell with 30 nm resolution. The experiments revealed that 80 nm oligomeric species convert to fibers of 1  $\mu m$  in length. [47]

Based on the data obtained in our study we propose an agglomeration pathway which is shown in Figure 4a. In the region free of visible aggregates (area 2) of Q72 cells, the GP model suggests the presence of flat aggregates with a thickness of ~170 Å and the p(r) analysis a thickness of ~180 Å. In the AFM results of in-vitro aggregated fibers discussed above<sup>[42,46]</sup> an oligomer size between 20 and 150 Å was found. Due to the similar size it is likely that the flat aggregates observed in the SAXS experiment are formed by the fibers found in AFM. The slightly larger size in SAXS experiments could be due to the incellulo environment which should differ from the in-vitro assembly conditions used in the AFM experiments or the way the fibers are stacked into the flat aggregates. These flat aggregates could then further stack as indicated by the second size in the p(r) analysis to form the larger aggregates detected by AFM.[42]

#### 5. Conclusion

Htt fibril and inclusion body formation is important for the pathogenesis of Huntingtin's disease and intensively studied by in vitro by fluorescence microscopy, in vitro or ex situ by AFM, and ex situ by electron microscopy. Here we established a complementary approach to analyze Huntingtin aggregates within frozen hydrated cells. We used cryo-SAXS which allows us to obtain within a nanofocus averaged information about the size and shape of intracellular structure in a native, hydrated environment. SAXS is inherently structure sensitive and we were able to obtain averaged information on structures present within the amyloid aggregates in the size range between 40 Å and 1,400 Å. The scattering data was analyzed via a Guinier-Porod model and p(r)-functions obtained by indirect Fourier transformation. Both, GP analysis and the IFT analysis clearly show the presence of agglomerated structures that result from the Q72 transfection that can be best described by flat objects. The thickness of these agglomerates of  $\approx$  170 Å fits well to previous in-vitro AFM results on Htt fiber formation and add the perception that fibers first form 2D assemblies prior to further growth into a 3D structure. We demonstrated that nanoprobe cryo-SAXS can serve as powerful tool to investigate aggregation processes of amyloid like aggregates inside cells and can be used in future experiments to understand the kinetics of fibril formation at different time points after transfection. In the future, studying the assembly and growth mechanism of Huntingtin aggregates as function of external stimuli and in the presence of drugs in-cellulo will help elucidating the aggregation mechanism of amyloid diseases to identify more effective drugs for such diseases. For in-vitro systems SAXS was capable

to reveal molecular insight into the aggregation process of amyloid fibers<sup>(48)</sup> While a future vision might be to follow similar approaches for entire cells, the approach is complicated by the crowded intracellular environment. Nevertheless, the combination of Cryogenic Nano-SAXS with Cryo-electron tomography (cryo-ET)<sup>(49)</sup> offers a promising perspective to study ß-sheet stacking and the influence of different drugs with relevance for the treatment of neurodegenerative diseases such as Huntington's disease.

# **Acknowledgements**

We acknowledge the excellent support during the beamtime from the Petra III staff and the team of the P10 beamline. Also, we acknowledge the support of Dr. Martin Schroer during data evaluation. The work was funded by the Virtual Institute VH-VI-403 (Helmholtz-Association), the Cluster of Excellence RESOLV (EXC 1069 and 2033, DFG) and BMBF (05K16PC1, 05K19PC2 and 05K16MG2). Stimulating discussions with Prof. R. Winter (TU Dortmund) are kindly acknowledged. Open access funding enabled and organized by Projekt DEAL.

## **Conflict of Interest**

The authors declare no conflict of interest.

**Keywords:** Huntington • inclusion bodies • nanodiffraction • neurodegeneration • small-angle X-ray scattering

- S. Büning, A. Sharma, S. Vachharajani, E. Newcombe, A. Ormsby, M. Gao, D. Gnutt, T. Vöpel, D. M. Hatters, S. Ebbinghaus, *Phys. Chem. Chem. Phys.* 2017, 19, 10738.
- [2] L. R. Gauthier, B. Né, D. C. Charrin, M. Borrell-Pagè, J. P. Dompierre, H. Lè Ne Rangone, F. P. Cordeliè Res, J. De Mey, M. E. Macdonald, V. Leßmann, S. Humbert, *IEEE Trans. Microwave Theory Tech.* 1982, 30, 845.
- [3] E. Cattaneo, Trends Neurosci. 2001, 24, 182.
- [4] E. Trushina, R. B. Dyer, J. D. Badger, D. Ure, L. Eide, D. D. Tran, B. T. Vrieze, V. Legendre-Guillemin, P. S. McPherson, B. S. Mandavilli, B. Van Houten, S. Zeitlin, M. McNiven, R. Aebersold, M. Hayden, J. E. Parisi, E. Seeberg, I. Dragatsis, K. Doyle, A. Bender, C. Chacko, C. T. McMurray, Mol. Cell. Biol. 2004, 24, 8195.
- [5] Y. C. Wong, E. L. F. Holzbaur, J. Neurosci. 2014, 34, 1293.
- [6] D. C. Rubinsztein, J. Leggo, R. Coles, E. Almqvist, V. Biancalana, J. Cassiman, K. Chotai, M. Connarty, D. Craufurd, A. Curtis, D. Curtis, M. J. Davidson, A. Differ, C. Dode, A. Dodge, M. Frontali, N. G. Ranen, C. Stine, M. Sherr, M. H. Abbott, M. L. Franz, C. A. Graham, P. S. Harper, J. C. Hedreen, A. Jackson, J. Kaplan, M. Losekoot, J. C. Macmillan, P. Morrison, Y. Trottier, A. Novelletto, S. A. Simpson, J. Theilmann, J. L. Whittaker, S. E. Folstein, C. A. Ross, M. R. Hayden, Am. J. Hum. Genet. 1996, 59, 16–22.
- [7] T. Vöpel, K. Bravo-Rodriguez, S. Mittal, S. Vachharajani, D. Gnutt, A. Sharma, A. Steinhof, O. Fatoba, G. Ellrichmann, M. Nshanian, C. Heid, J. A. Loo, F.-G. Klärner, T. Schrader, G. Bitan, E. E. Wanker, S. Ebbinghaus, E. Sanchez-Garcia, J. Am. Chem. Soc. 2017, 139, 5640.
- [8] S. Sinha, D. H. J. Lopes, Z. Du, E. S. Pang, A. Shanmugam, A. Lomakin, P. Talbiersky, A. Tennstaedt, K. McDaniel, R. Bakshi, P.-Y. Kuo, M. Ehrmann, G. B. Benedek, J. A. Loo, F.-G. Klärner, T. Schrader, C. Wang, G. Bitan, J. Am. Chem. Soc. 2011, 133, 16958.
- [9] H. J. Wobst, A. Sharma, M. I. Diamond, E. E. Wanker, J. Bieschke, FEBS Lett. 2015, 589, 77.



- [10] J. Bieschke, M. Herbst, T. Wiglenda, R. P. Friedrich, A. Boeddrich, F. Schiele, D. Kleckers, J. M. Lopez del Amo, B. A. Grüning, Q. Wang, M. R. Schmidt, R. Lurz, R. Anwyl, S. Schnoegl, M. Fändrich, R. F. Frank, B. Reif, S. Günther, D. M. Walsh, E. E. Wanker, *Nat. Chem. Biol.* 2012, 8, 93.
- [11] D. I. Svergun, M. H. J. Koch, Rep. Prog. Phys. 2003, 66, 1735.
- [12] C. E. Blanchet, D. I. Svergun, Annu. Rev. Phys. Chem. 2013, 64, 37.
- [13] M. Granke, A. Gourrier, F. Rupin, K. Raum, F. Peyrin, M. Burghammer, A. Saied, PLoS ONE 2013, 8, 3.
- [14] A. R. von Gundlach, V. M. Garamus, T. Gorniak, H. A. Davies, M. Reischl, R. Mikut, K. Hilpert, A. Rosenhahn, *Biochim. Biophys. Acta Biomembr.* 2016, 1858, 918.
- [15] T. Gorniak, T. Haraszti, V. M. Garamus, A. R. Buck, T. Senkbeil, M. Priebe, A. Hedberg-Buenz, D. Khoen, T. Salditt, M. Grunze, M. G. Anderson, A. Rosenhahn, *PLoS One* 2014, 9, DOI 10.1371/journal.pone.0090884.
- [16] B. Weinhausen, O. Saldanha, R. N. Wilke, C. Dammann, M. Priebe, M. Burghammer, M. Sprung, S. Köster, Phys. Rev. Lett. 2014, 088102, 1.
- [17] S. Kasas, G. Dumas, G. Dietler, S. Catsicas, M. Adrian, J. Microsc. 2003, 211, 48.
- [18] S. Kalbfleisch, H. Neubauer, S. P. Krüger, M. Bartels, M. Osterhoff, D. D. Mai, K. Giewekemeyer, B. Hartmann, M. Sprung, T. Salditt, I. McNulty, C. Eyberger, B. Lai, in AIP Conf. Proc., 2011, pp. 96–99.
- [19] T. Salditt, S. Kalbfleisch, M. Osterhoff, S. P. Krüger, M. Bartels, K. Giewekemeyer, H. Neubauer, M. Sprung, Opt. Express 2011, 19, 9656.
- [20] T. Salditt, M. Osterhoff, M. Krenkel, R. N. Wilke, M. Priebe, M. Bartels, S. Kalbfleisch, M. Sprung, J. Synchrotron Radiat. 2015, 22, 867.
- [21] J. Ilavsky, P. R. Jemian, J. Appl. Crystallogr. 2009, 42, 347.
- [22] B. Hammouda, J. Appl. Crystallogr. 2010, 43, 716.
- [23] O. Glatter, J. Appl. Crystallogr. 1977, 10, 415.
- [24] P. V. Konarev, V. V. Volkov, A. V. Sokolova, M. H. J. Koch, D. I. Svergun, J. Appl. Crystallogr. 2003, 36, 1277.
- [25] D. Franke, M. V. Petoukhov, P. V. Konarev, A. Panjkovich, A. Tuukkanen, H. D. T. Mertens, A. G. Kikhney, N. R. Hajizadeh, J. M. Franklin, C. M. Jeffries, D. I. Svergun, J. Appl. Crystallogr. 2017, 50, 1212.
- [26] L. Mangiarini, K. Sathasivam, M. Seller, B. Cozens, A. Harper, C. Hetherington, M. Lawton, Y. Trottier, H. Lehrach, S. W. Davies, G. P. Bates, Cell 1996, 87, 493.
- [27] W. F. Tivol, A. Briegel, G. J. Jensen, *Microsc. Microanal.* **2008**, *14*, 375.
- [28] P. Hawkes, J. Spence, Science of Microscopy, Springer New York, New York, NY, 2007.
- [29] T. Gorniak, T. Haraszti, H. Suhonen, Y. Yang, A. Hedberg-Buenz, D. Koehn, R. Heine, M. Grunze, A. Rosenhahn, M. G. Anderson, *Pigm. Cell Res.* 2014, 27, 831.
- [30] S. Matsuyama, M. Shimura, M. Fujii, K. Maeshima, H. Yumoto, H. Mimura, Y. Sano, M. Yabashi, Y. Nishino, K. Tamasaku, Y. Ishizaka, T. Ishikawa, K. Yamauchi, X-Ray Spectrom. 2010, 39, 260.

- [31] T. Gorniak, T. Haraszti, V. M. Garamus, A. R. Buck, T. Senkbeil, M. Priebe, A. Hedberg-Buenz, D. Koehn, T. Salditt, M. Grunze, M. G. Anderson, A. Rosenhahn, *PLoS One* 2014, 9, e90884.
- [32] J. Dubochet, M. Adrian, J.-J. Chang, J.-C. Homo, J. Lepault, A. W. McDowall, P. Schultz, Q. Rev. Biophys. 1988, 21, 129.
- [33] J. L. S. Milne, M. J. Borgnia, A. Bartesaghi, E. E. H. Tran, L. A. Earl, D. M. Schauder, J. Lengyel, J. Pierson, A. Patwardhan, S. Subramaniam, FEBS J. 2013, 280, 28.
- [34] V. R. F. Matias, T. J. Beveridge, Mol. Microbiol. 2005, 56, 240.
- [35] P. W. Schmidt, in Mod. Asp. Small-Angle Scatt. (Ed: H. Brumberger), Springer Netherlands, Dordrecht, 1995, pp. 1–56.
- [36] H. Schnablegger, Y. Singh, Ant. Paar 2011.
- [37] B. Hammouda, PROBING NANOSCALE STRUCTURES THE SANS TOOLBOX, n.d.
- [38] H. Kawasaki, V. M. Garamus, M. Almgren, H. Maeda, J. Phys. Chem. B 2006, 110, 10177.
- [39] S. Chimon, M. A. Shaibat, C. R. Jones, D. C. Calero, B. Aizezi, Y. Ishii, Nat. Struct. Mol. Biol. 2007, 14, 1157.
- [40] P. R. Dahlgren, M. A. Karymov, J. Bankston, T. Holden, P. Thumfort, V. M. Ingram, Y. L. Lyubchenko, *Nanomedicine Nanotechnology, Biol. Med.* 2005, 1, 52.
- [41] A. Der-Sarkissian, C. C. Jao, J. Chen, R. Langen, J. Biol. Chem. 2003, 278, 37530.
- [42] K. A. Burke, J. Godbey, J. Legleiter, Methods 2011, 53, 275.
- [43] M. A. Poirier, H. Li, J. Macosko, S. Cai, M. Amzel, C. A. Ross, J. Biol. Chem. 2002, 277, 41032.
- [44] J. L. Wacker, M. H. Zareie, H. Fong, M. Sarikaya, P. J. Muchowski, *Nat. Struct. Mol. Biol.* **2004**, *11*, 1215.
- [45] M. Tanaka, I. Morishima, T. Akagi, T. Hashikawa, N. Nukina, J. Biol. Chem. 2001, 276, 45470.
- [46] J. Legleiter, E. Mitchell, G. P. Lotz, E. Sapp, C. Ng, M. DiFiglia, L. M. Thompson, P. J. Muchowski, J. Biol. Chem. 2010, 285, 14777.
- [47] W. C. Duim, Y. Jiang, K. Shen, J. Frydman, W. E. Moerner, ACS Chem. Biol. 2014, 9, 2767.
- [48] A. E. Langkilde, K. L. Morris, L. C. Serpell, D. I. Svergun, B. Vestergaard, Acta Crystallogr. Sect. D 2015, 71, 882.
- [49] J. Mahamid, S. Pfeffer, M. Schaffer, E. Villa, R. Danev, L. K. Cuellar, F. Förster, A. A. Hyman, J. M. Plitzko, W. Baumeister, *Science* 2016, 351, 969.

Manuscript received: October 30, 2020 Accepted manuscript online: December 18, 2020 Version of record online: January 27, 2021